



Effect of chest physiotherapy on cystic fibrosis sputum nanostructure: an experimental and theoretical approach

Michela Abrami¹ · Massimo Maschio² · Massimo Conese³ · Marco Confalonieri⁴ · Francesco Salton⁴ · Fabio Gerin⁵ · Barbara Dapas⁵ · Rossella Farra⁶ · Alessandra Adrover⁷ · Gesmi Milcovich⁸ · Claudia Fornasier⁵ · Alice Biasin¹ · Mario Grassi¹ · Gabriele Grassi⁵

Accepted: 4 February 2022 / Published online: 14 March 2022
© The Author(s) 2022, corrected publication 2022

Abstract

Cystic fibrosis (CF) is a disease characterized by the production of viscous mucoid secretions in multiple organs, particularly the airways. The pathological increase of proteins, mucin and biological polymers determines their arrangement into a three-dimensional polymeric network, affecting the whole mucus and impairing the muco-ciliary clearance which promotes inflammation and bacterial infection. Thus, to improve the efficacy of the drugs usually applied in CF therapy (e.g., mucolytics, anti-inflammatory and antibiotics), an in-depth understanding of the mucus nanostructure is of utmost importance. Drug diffusivity inside a gel-like system depends on the ratio between the diffusing drug molecule radius and the mesh size of the network. Based on our previous findings, we propose the combined use of rheology and low field NMR to study the mesh size distribution of the sputum from CF patients. Specifically, we herein explore the effects of chest physiotherapy on CF sputum characteristic as evaluated by rheology, low field NMR and the drug penetration through the mucus via mathematical simulation. These data show that chest physiotherapy has beneficial effects on patients, as it favourably modifies sputum and enhances drug penetration through the respiratory mucus.

Keywords Cystic fibrosis · Sputum · Rheology · Low field NMR · Mesh size distribution · Drug delivery

✉ Mario Grassi
mario.grassi@dia.units.it

- ¹ Department of Engineering and Architecture, University of Trieste, Via Valerio 6/A, 34127 Trieste, Italy
- ² Institute for Maternal and Child Health, IRCCS Burlo Garofolo, Via dell Istria, 65, 34137 Trieste, Italy
- ³ Department of Medical and Surgical Sciences, Foggia University, Ospedali Riuniti, Via L. Pinto, 1, 71122 Foggia, Italy
- ⁴ Pulmonology Department, Cattinara University Hospital, Strada di Fiume 447, 34149 Trieste, Italy
- ⁵ Department of Life Sciences, Cattinara University Hospital, Trieste University, Strada di Fiume 447, 34149 Trieste, Italy
- ⁶ Clinical Department of Medical, Surgical and Health Sciences, Cattinara University Hospital, Trieste University, Strada di Fiume 447, 34149 Trieste, Italy
- ⁷ Department of Chemical Engineering, Materials and Environment, Sapienza University of Roma, Via Eudossiana 18, 00184 Rome, Italy
- ⁸ School of Chemical Sciences, Dublin City University (DCU), Dublin, Ireland

Introduction

Cystic fibrosis (CF) is one of the most common lethal genetic diseases in people of Caucasian origin [1, 2]. The disease is caused by mutations in the gene encoding the cystic fibrosis transmembrane conductance regulator (CFTR). The CFTR gene encodes an *ATP*-regulated chloride channel present within the apical surface of epithelial cells. Dis-functional CFTR determines a decreased surface liquid volume and increased mucus viscosity in many organs, mainly to the airway. In the healthy lungs, inhaled particles are transported out of the lung by cilia movement, within a process called muco-ciliary clearance. The increased viscosity of mucus in CF patients impairs muco-ciliary clearance determining mucus stagnation, thus favouring bacterial lung infections, a typical event in CF patients [2]. In this regard, CF patients are often colonized by *S. aureus* in the early childhood [3]. *S. aureus* is replaced during disease progression by *P. aeruginosa* as the dominant pathogen. By the time of reaching adulthood, up to 80% of CF patients are chronically infected by *P. aeruginosa*. These chronic pulmonary infections are

associated with a rapid decline in lung functions, high morbidity and short life expectancy [4]. One of the most striking hallmarks of *P. aeruginosa* in chronically infected CF patients is the conversion to a mucoid phenotype of the mucus due to the increased production of alginates [5–7], natural polymers composed of mannuronic and guluronic acid units arranged in a block-wise pattern [8]. Alginates overproduction can contribute to a strong inflammatory response sustained by immune cells that can influence lung epithelial cells [9–11]. During inflammation, substances like proteins, mucin and biological polymers increase in mucus as well as the increased alginate production. These compounds organize into a three-dimensional polymeric network, affecting the whole mucus, impairing the muco-ciliary clearance, promoting bacterial infection and hindering drug diffusion to the epithelial cells.

The nanostructure of the network requires an in-depth understanding, in order to improve the efficacy of the drugs usually employed in CF therapy (e.g., mucolytics, anti-inflammatory and antibiotics) when administered alone or in combination with chest physiotherapy. Indeed, drug diffusivity inside a gel-like system depends on the ratio between the diffusing drug molecule radius and the network mesh size. This parameter has driven several research studies focus to date, due to its relevance on the CF sputum/mucus properties [12]. Hanes et al. demonstrated that sputum/mucus is a heterogeneous medium made up of mainly physical cross-linked polymeric regions, embedded in a low viscosity, water-like and fluid [12–14]. According to their complex structure, both the macro- and the micro-rheological mucus/sputum properties have been studied by classical strain/stress controlled rheometers and an innovative particle tracking approach [13]. The network mesh size was determined relating on rheological sputum characteristics [14] and probe particles tracking [15]. However, as clearly pointed out by Bhat and co-workers [16–18], drug diffusion through mucus can be also affected by drug binding to the glycoproteins. In addition, drug action can be reduced by non-physiological ionic strength, pH, mucociliary clearance and biochemical alterations of mucus [18].

Based on our previous findings, we herein propose the synergic combination of rheology and low-field nuclear magnetic resonance (*LF-NMR*) to study the mesh size distribution changes of mucus in CF patients (obtained by voluntary expectoration and from now on called “sputum”), prior and after chest physiotherapy. Indeed, while *LF-NMR* can provide for info about sputum structure, depending on the magnetic relaxation of water hydrogen trapped in the network, rheology can yield to further insights on the nanostructure, relating on the mechanical relaxation of the polymeric network chains. Furthermore, *LF-NMR* allows determining the spin–spin relaxation time (T_{2m}) of the water hydrogens, whereas rheology allows measuring

the shear modulus G of the sputum. Remarkably, it is possible to determine important features of the sputum nanostructure and further develop innovative drug penetration range, on the T_{2m} and G knowledge. In particular, the present work focuses on the effects that chest physiotherapy has on sputum characteristic lean on rheology/*LF-NMR* analysis. Therefore, we hypothesize that chest physiotherapy can also influence the sputum nanostructure, representing a pivotal information for clinicians in order to optimize the therapy, for future precision and personalized medicine approach.

Materials and methods

Samples collection

Sputum samples were provided by the Burlo Garofolo Hospital, following a procedure approved by the Ethics Committee (prot n. 496/2916, CI M-11, 22–3-2016). Written informed consent was obtained from each patient. One sputum specimen was collected before and after chest physiotherapy session in randomly selected adult and young patients able to expectorate. Non-expectorant patients were excluded, as were subjects ≤ 7 years of age. The chest physiotherapy technique is set up on patient to patient even if the technique most used for the patients enrolled in this study is the pep-mask. Sometimes, autogenous drainage has also been used. Chest physiotherapy was provided as standard procedure for CF patients, to improve clearance, both by using positive expiratory pressure devices and standardised physiotherapist-guided chest applied manoeuvres, as well as effective breathing exercise [19].

The aforementioned criteria allowed for the recruitment of most patients who attended Burlo Garofolo Hospital for a clinical visit during our study period (from January 2019 to December 2020). Spontaneously expectorated (1–2 mL) sputum was collected from CF patients in sterile cups and immediately used for T_{2m} determination. The samples were then transferred from the *LF-NMR* glass tube to a rheometer device for analysis. Patient’s lung functionality, performed after chest physiotherapy, was evaluated by the Burlo Garofolo Hospital by means of FEV_1 (forced expiratory volume in the first second), i.e. the volume of air that can be forced out in one second after taking a deep breath.

Rheology

The viscoelastic properties of the analysed samples were determined by means of two rheological tests called, respectively, *stress sweep* and *frequency sweep* test. These experiments require the application of a sinusoidal stress (τ) to the sample in order to measure the related oscillatory deformation (γ). *Stress sweep* tests were lead applying a sinusoidal

stress of constant frequency ($f=1$ Hz) and increasing amplitude to detect the limit of the linear viscoelastic range. *Frequency sweep* tests, performed in the linear viscoelastic range, as to prevent any sample structure damaging, were lead in the frequency range 10–0.01 Hz. The output of the frequency sweep tests, i.e. the elastic (G') and viscous (G'') moduli dependence on pulsation $\omega (=2\pi f)$ (mechanical spectrum), were fitted by the generalized Maxwell model [20]:

$$G' = \sum_{i=1}^{n_R} g_i \frac{(\lambda_i \omega)^2}{1 + (\lambda_i \omega)^2} \tag{1}$$

$$G'' = \sum_{i=1}^{n_R} g_i \frac{(\lambda_i \omega)}{1 + (\lambda_i \omega)^2} \tag{2}$$

where n_R is the number of Maxwell elements considered, whereas g_i (ith elastic constant), η_i (ith viscosity) and λ_i (ith relaxation time) represent model fitting parameters. Model fitting was performed assuming that λ_i were scaled by a factor 10 ($\lambda_{i+1} = 10 \lambda_i$) [20]. Although other fitting strategies could have been followed, this approach enables getting a wider and, thus, clearer, relaxation spectrum (g_i vs λ_i). The n_R determination was performed according to a statistical procedure, in order to minimize the product $N^* \chi^2$, where N indicates the number of fitting parameters and χ^2 is the sum of the squared errors [21]). The sample shear modulus G was evaluated as the sum of all g_i ($G = \sum g_i$) [22]. Therefore, Flory theory [23] allows to evaluate the polymeric network crosslink density, ρ_x , defined as the moles of junction points between different polymeric chains per hydrogel unit volume, based on previous G determination:

$$T_{2m} = \sum_{i=1}^m A_i T_{2i} / \sum_{i=1}^m A_i \quad \left(\frac{1}{T_2} \right)_m = \sum_{i=1}^m \frac{A_i}{T_{2i}} / \sum_{i=1}^m A_i \quad A_i\% = 100 A_i / \sum_{i=1}^m A_i \tag{6}$$

$$\rho_x = G/RT \tag{3}$$

where R is the universal gas constant and T is the absolute temperature. Therefore, the equivalent network theory [24] enables the determination of the average mesh size ξ_a :

$$\xi_a = \sqrt[3]{6/\pi \rho_x N_A} \tag{4}$$

where N_A is the Avogadro number.

Low-field NMR

NMR is based on hydrogen atoms dipole reaction to the external constant magnetic field (B_0) switch where they are embedded. Indeed, inside B_0 , hydrogen atoms dipoles tend to line up in the B_0 direction so that, globally, they give origin

to the induced magnetization vector M , oriented in the B_0 direction. Due to B_0 perturbation, realized by the application of a proper radio frequency pulse B_1 perpendicular to B_0 , M rotates in the XY plane of B_1 (that perpendicular to B_0). Upon B_1 removal, M tends to line up again to the B_0 direction (relaxation) so that its XY component (M_{XY}) diminishes with time and its component in the B_0 direction (conventionally the vertical or Z one; M_z) increases in time. The mathematical description of the relaxation process (i.e. the M_{XY} time reduction) is given by the solution of the magnetization diffusion equation proposed by Brownstein and Tarr [25, 26]:

$$I(t) = \sum_{i=1}^m A_i e^{-(t/T_{2i})} \tag{5}$$

where t is time, $I(t)$ is the ratio between the time dependent value of M_{XY} and its maximum value (M_{XYmax}) occurring just after B_1 removal, T_{2i} represent the i th spin–spin or transverse relaxation times, while A_i are “weights” proportional to the number of hydrogen atoms whose dipoles relaxation is characterized by T_{2i} . Equation (5) simply states that the relaxation process is the result of “ m ” exponential relaxation processes each one characterized by its own relaxation time (T_{2i}) and weight (A_i). The determination of the unknown couples (T_{2i} , A_i) was performed by Eq. (5) fitting to the experimental $I(t)$ values ($I_s(t)$), and the number, m , of exponential decays appearing in Eq. (5) was determined per the statistics applied in the Rheology section [21].

The average relaxation time (T_{2m}) and the average inverse relaxation time ($(1/T_2)_m$), depending on several variables such as temperature, B_0 strength, and the presence of a disperse phase in the system as it happens in hydrogel system [26], can be defined by:

when T_{2m} is evaluated as the inverse of $(1/T_2)_m$, it is named T_{2mb} .

While Eq. (5) provides the discrete relaxation time distribution represented by the m couples ($A_i\%-T_{2i}$), it is possible to determine the continuous distribution according to what suggested by Whittall and MacKay [27]:

$$I(t) = \int_{T_{2min}}^{T_{2max}} a(T_2) \exp\left\{-\frac{t}{T_2}\right\} dT_2 \tag{7}$$

where T_{2max} ($=10^4$ ms) and T_{2min} ($=0.1$ ms) indicate, respectively, the lower and upper values of the continuous T_2 distribution, $a(T_2)$ is the unknown amplitude of the spectral component at the relaxation time T_2 , while $\exp\{-t/T_2\}$ represents the decay term. Equation (7) represents the “continuous” expression of Eq. (5). This means that while Eq. (5) describes the M_{XY} relaxation process by means of a limited

(discrete) number of initially unknowns T_{2i} , Eq. (7) makes use of a much higher number of known relaxation times belonging to the interval $(T_{2\min} - T_{2\max})$ and comprehending all the possible relaxation times characterizing the sample under study (continuous distribution of relaxation times).

In order to fit the experimental M_{XY} time decay $I_s(t)$ by Eq. (7) and get the continuous T_2 distribution (the unknowns $A_i = a_i(T_{2i}) * \Delta T_{2i}$), the following discretization was applied [27]:

$$I(t) \approx \sum_{i=1}^N a_i e^{\left\{-\frac{t}{T_{2i}}\right\}} (T_{2i+1} - T_{2i}) = \sum_{i=1}^N A_i e^{\left\{-\frac{t}{T_{2i}}\right\}} \quad (8)$$

where the range of the T_2 distribution $(T_{2\min} - T_{2\max})$ was logarithmically subdivided into $N=200$ parts (higher N values were unnecessary). Because of the noise disturbing the measure of I_s , the fitting procedure must not minimize the χ^2 statistic, but a smoothed definition of it (χ_s^2) [27]:

$$\chi_s^2 = \sum_{i=1}^N \left(\frac{I_s(t_i) - I(t_i)}{\sigma_i} \right)^2 + \mu \sum_{i=1}^{N-2} |A_{i+2} - 2A_{i+1} + A_i|^2 \quad (9)$$

where σ_i is the i^{th} datum standard deviation and μ is the weight of the smoothing term (second summation in Eq. (9)) proposed by Provencher [28]. Although different criteria can be used to determine μ , the strategy proposed by Wang [29] was applied. Based on this strategy, the correct μ value is that occurring just below the heel (slope variation) of the function $\ln(\chi_s)$ vs $\ln(\mu)$. In the present work, $\mu=150$ was determined.

The discrete and continuous T_2 distribution can be transformed into hydrogel mesh size distribution resorting to one of the fundamental relations of the low-field NMR field. This relation, based on the solution of the magnetization diffusion equation proposed by Brownstein and Tarr [25, 26], establishes the link between $(1/T_2)_m$ and the ratio of the surface (S) of the dispersed/solubilized substances in the sample and the volume (V) of the sample water molecules:

$$\left(\frac{1}{T_2} \right)_m = \frac{1}{T_{2H_2O}} + \frac{S}{V} M \quad (10)$$

where T_{2H_2O} is the bulk protons relaxation time (i.e. the water proton relaxation time in the absence of polymer, the so-called free water relaxation time ≈ 3700 ms at 37°C and $B_0=0.47$ T [30]) and M (length/time) is a physical parameter, named relaxivity, which represents the effect of the surface of polymer chains on water proton relaxation. Indeed, M is equal to the ratio between thickness and relaxation time of the bound water layer adhering to the solid surface. Equation (10), stating that $(1/T_2)_m$ depends on (S/V) , clearly establishes the relation between the relaxation time and

the spatial organization of the sample network that heavily affects the S/V ratio [26]. For instance, in many polymeric systems, crosslinking induces a spatial reorganization of the polymeric chains contained in the original solution that involves the increase of the ratio S/V [31, 32]. This, in turn, reflects in the increase of $(1/T_2)_m$ and in the decrease of T_{2m} .

Despite its theoretical importance, Eq. (10) can be rewritten in a more useful form, based on the fibre cell [26] and Scherer theories [33]. At this purpose, Abrami et al. [34] demonstrated that, for a hydrogel polymer volume fraction $\phi < 0.6$, the term (S/V) can be expressed as a function of the average mesh size ξ_a of the polymeric network (error $< 5\%$):

$$\frac{S}{V} = \frac{2}{\xi_a \sqrt{\frac{C_0}{C_1} \frac{1-0.58\phi}{\phi}}} \quad (11)$$

where C_0 and C_1 are two constants depending on the mesh architecture and equal, respectively, to 1 and 3π in the case of cubic mesh [33]. Thus, Eq. (10) becomes

$$\left(\frac{1}{T_2} \right)_m = \frac{1}{T_{2H_2O}} + 2 \frac{M}{\xi_a \sqrt{\frac{C_0}{C_1} \frac{1-0.58\phi}{\phi}}} \quad (12)$$

while Eq. (12) refers, averagely, to all the polymeric network meshes, similar expressions can be written for meshes of different dimensions (ξ_i), assuming the M independence on the mesh size [26]:

$$\frac{1}{T_{2i}} = \frac{1}{T_{2H_2O}} + 2 \frac{M}{\xi_i \sqrt{\frac{C_0}{C_1} \frac{1-0.58\phi}{\phi}}} \quad (13)$$

where T_{2i} is the relaxation time of water protons trapped in polymer meshes of size ξ_i . The bi-univocal correspondence between T_{2i} and ξ_i only holds in the fast-diffusion regime (typical of gels), i.e. when the mobility of water molecules, expressed by their self-diffusion coefficient D (3.04×10^{-9} m²/s at 37°C [35]), is large whether compared to the rate of magnetization loss ($R_c \times M$) (i.e. $R_c * M/D \ll 1$). In the slow diffusion regime, relaxation of all the water protons contained in the volume of a mesh of size ξ_i is not described by just one T_{2i} but several T_{2i} . R_c indicates the radial distance from the polymer chain axis where the effect of polymeric chains on water proton relaxation becomes negligible. This can be expressed by [26]

$$R_c = \frac{r_f}{\sqrt{\phi}} \quad (14)$$

The combination of Eqs. (12) and (13) allows to conclude that the ratio between ξ_i and its average value, ξ_a , depends exclusively on the relaxation times T_{2i} and T_{2m} (except for the free water relaxation time T_{2H_2O}):

$$\xi = \xi_a \frac{\left(\left(\frac{1}{T_2} \right)_m - \frac{1}{T_{2H_2O}} \right)}{\left(\frac{1}{T_{2i}} - \frac{1}{T_{2H_2O}} \right)} \tag{15}$$

Thus, Eq. (5) or Eq. (8) fitting to experimental M_{XY} decay ($I_s(t)$) allows determining the discrete or continuous relaxation spectrum ($A_{i\%} - T_{2i}$), whereas Eq. (13) provides for the conversion into the discrete or continuous mesh size distribution of the sputum ($A_{i\%} - \xi_i$).

LF-NMR measurements were performed at 37 °C by means of a Bruker Minispec mq20 (0.47 T, Germany). The determination of T_{2m} was performed according to the CPMG sequence (Carr–Purcell–Meiboom–Gill) [36] $\{90^\circ[-\tau-180^\circ-\tau(\text{echo})]n-T_R\}$ with a 8.36 μs wide 90° pulse, $\tau = 250 \mu\text{s}$, and T_R (sequences repetition rate) equal to 10 s. In order to obtain the final I_s of 2%, the proper n was chosen. m was determined according to the statistics applied in the Rheology section [21]. Each spin-echo decay, composed by n points, was repeated 36 times (number of scans).

Drug diffusion

The walls of the bronchial tree are covered by a very thin layer of a water-like serous fluid, the periciliary liquid (PCL), where cells cilia beat with a typical frequency of 20 Hz and amplitude about 5 μm . On the top of PCL, a thin layer of a non-Newtonian viscoelastic fluid lies, named mucus [37] (see Fig. 1).

PCL and mucus layer (ML) constitute the airway surface liquid (ASL) [38]. The viscoelastic nature of mucus depends on the presence of different components such as proteins, alginates, white blood cells, DNA, bacteria and mucin (whose levels are pathologically increased compared with healthy subjects [39]) that lead to a three-dimensional network [40]. Drug permeation inside the ASL is a complex phenomenon affected by many factors such as the thickness of ASL, which depends on the ASL rheological properties and the airflow [37, 41, 42]. Moreover, possible interactions (e.g. electrostatic and hydrogen bonding) between the diffusing drug and the polymeric components of the ALS cannot be a priori excluded [43]. Furthermore, as ASL is not homogeneous, the drug diffusion coefficient (D) should be position dependent [42]. However, assuming that drug transport is mainly affected by diffusion with constant D , the prediction of the drug penetration inside ASL can be obtained by referring to the one-dimensional Fick’s equation with proper initial and boundary conditions. In detail, it is assumed that at time zero (deposition of drug solution on ASL, following inhalation), the drug is not present inside ASL, and it is uniformly distributed, at the known concentration C_0 , in the solution layer of thickness δ (see Fig. 1). Boundary conditions involve the existence of an impermeable wall in $X=0$

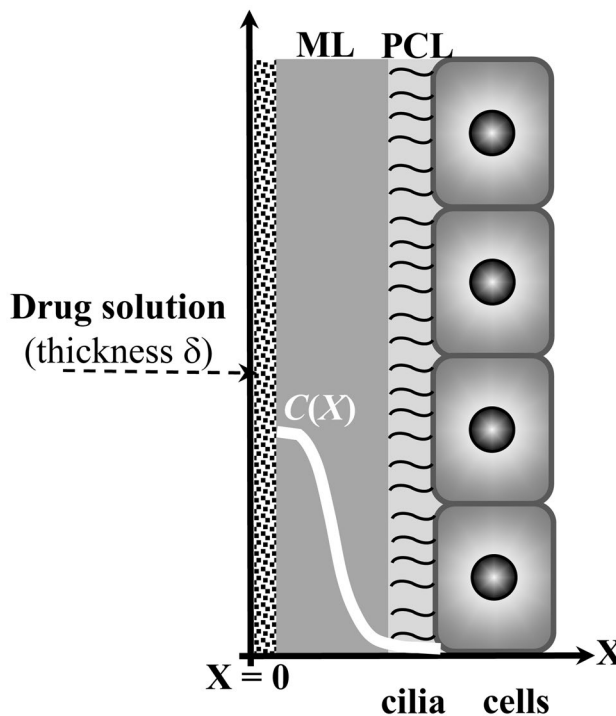


Fig. 1 The airway surface liquid (ASL) lining the walls of the bronchial tree is composed by the periciliary liquid (PL), where cells cilia beat, and by the mucus layer (ML). When a drug solution is inhaled, it spreads on the ML, and the drug can diffuse inside the ASL. White line indicates the hypothetical drug concentration profile inside ASL

(the drug cannot diffuse in the X negative direction) and the possibility of drug diffusion in the positive X direction up to infinite (therefore, the drug can diffuse inside cells, too). According to these hypotheses, the time evolution of the drug profile concentration (C) inside ASL is determined by

$$\frac{C}{C_0} = \frac{\delta}{\sqrt{Dt\pi}} e^{-\left(\frac{X^2}{4Dt}\right)} \tag{16}$$

where t is time. The D value to be used in Eq. (15) can be provided by the Lusting-Peppas equation [44] as per Abrami et al. [23]:

$$D = D_0 \left(1 - \frac{2r_s}{\xi_a}\right) e^{-Y\left(\frac{\phi}{1-\phi}\right)} \tag{17}$$

where r_s is the radius of the drug molecule imagined to be a sphere, D_0 is the drug diffusion coefficient in water, while Y is a model parameter that, lacking further information, can be set equal to 1 [44], although it usually ranges between 3 and 30 [45, 46] (see Appendix 1 for some considerations on the potentiality of Eq. (17)). The solid volume fraction ϕ was set equal to 0.05, this being the most common situation, albeit variability can occur among samples [47]. For what concerns r_s and D_0 , with an attention focus on typical

antibiotics used for *FC* patients (ciprofloxacin and tobramycin, for example [48]), reasonable values are 1.1 nm and $3 \times 10^{-10} \text{ m}^2/\text{s}$, respectively [49, 50]. Moreover, it is worth mentioning that while the *PCL* thickness ranges between 5 and 10 μm [51], in healthy subjects and in *CF* patients, *ML* thickness is similar and, approximately, equal to 25–30 μm [37, 52]. Vice-versa, patients affected by chronic obstructive pulmonary diseases (COPD) exhibit an *ML* thickness value up to 300 μm [41].

Statistical analysis

The nature of the experimental data distribution (normal or not) was evaluated by the Kolmogorov–Smirnov test (KS-test). Based on KS-test results, the Spearman's correlation coefficient (r_{sp}) was considered to verify possible direct or inverse correlations among T_{2m} , FEV_1 and G . Correlations among variables were considered significant when $p < 0.05$, corresponding to a probability of 95%. Lower probability was associated to a lack of correlation among variables.

Results and discussion

Figure 2 remarkably shows that there is a statistically significant correlation between T_{2m} measured in *CF* sputum and FEV_1 before (dark circles; $r_{sp} = 0.69$, $p = 0.006$) and after (white circles; $r_{sp} = 0.44$, $p = 0.044$) chest physiotherapy. As lung functionality increases with FEV_1 [53], Fig. 2 indicates that T_{2m} increase is connected with improved patient clinical

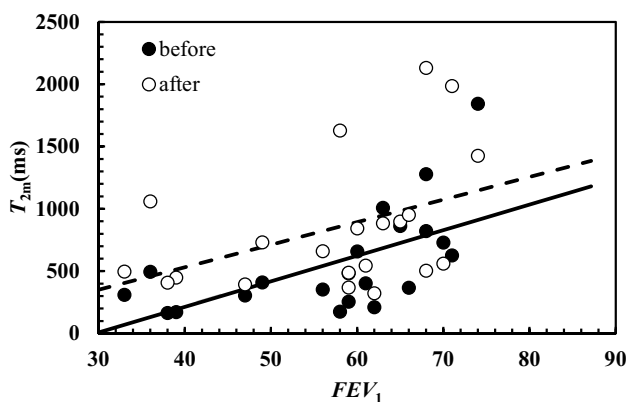


Fig. 2 Correlation between T_{2m} and FEV_1 before (black circles) and after (white circles) chest physiotherapy. In both cases, the correlation is statistically significant (before: $r_{sp} = 0.69$, $p = 0.006$; after $r_{sp} = 0.44$, $p = 0.044$). The linear relation occurring between T_{2m} and FEV_1 is represented by solid line (before: $T_{2m}(\text{ms}) = (20.5 \pm 6.3) \times FEV_1 - (609 \pm 366)$) and dashed line (after: $T_{2m}(\text{ms}) = (18.1 \pm 9.0) \times FEV_1 - (193 \pm 526)$)

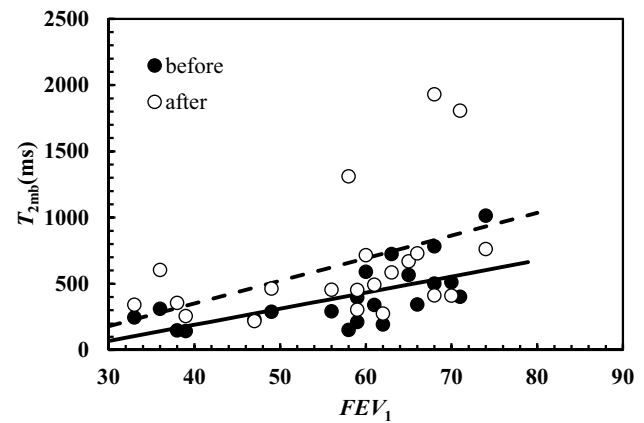


Fig. 3 Correlation between T_{2mb} and FEV_1 before (dark circles) and after (white circles) chest physiotherapy. In both cases, the correlation is statistically significant (before: $r_{sp} = 0.73$, $p = 0.0002$; after $r_{sp} = 0.51$, $p = 0.019$). The linear relation occurring between T_{2mb} and FEV_1 is represented by solid line (before: $T_{2mb}(\text{ms}) = (12.2 \pm 3.3) \times FEV_1 - (295 \pm 195)$) and dashed line (after: $T_{2mb}(\text{ms}) = (17.1 \pm 8.0) \times FEV_1 - (333 \pm 464)$)

conditions. Moreover, the inspection of Fig. 2 reveals that, on average, after chest physiotherapy, T_{2m} is higher.

Indeed, the dashed line (connected with the T_{2m} vs FEV_1 trend after chest physiotherapy) is characterized by a higher intercept with respect to solid line (connected with the T_{2m} vs FEV_1 trend before chest physiotherapy), and the two straight lines share, approximately, the same slope. Thus, the beneficial action of chest physiotherapy is clearly evident.

Interestingly, similar correlations between T_{2mb} (average relaxation time evaluated as the inverse of $(1/T_{2m})$) and FEV_1 have been determined both before and after chest physiotherapy as shown on Fig. 3.

This finding is due to the strong correlation existing between T_{2m} and T_{2mb} ($r_{sp} = 0.97$, $p < 0.0001$), as per Fig. 4

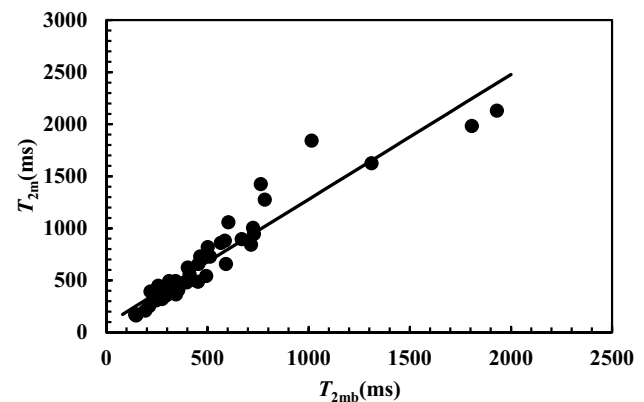


Fig. 4 Statistically significant correlation between T_{2m} and T_{2mb} referring to all the 42 samples considered ($r_{sp} = 0.97$, $p < 0.0001$). Solid line represents the linear interpolant: $T_{2m}(\text{ms}) = (1.2 \pm 0.06) \times T_{2mb} + (78 \pm 41)$

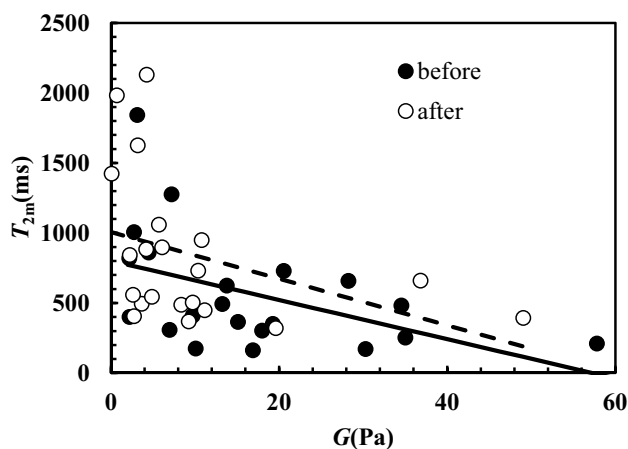


Fig. 5 Correlation between T_{2m} and G . Dark circles indicate samples before chest physiotherapy, while white circles refer to samples after chest physiotherapy. A statistically significant correlation between T_{2m} and G occurs both before ($r_{sp} = -0.53$, $p = 0.014$; $T_{2m}(\text{ms}) = -(14.0 \pm 6.0) \times G(\text{Pa}) + (801 \pm 131)$; solid line) and after ($r_{sp} = -0.495$, $p = 0.023$; $T_{2m}(\text{ms}) = -(14.6 \pm 9.3) \times G(\text{Pa}) + (1006 \pm 143)$; dashed line) chest physiotherapy. The overall correlation is statistically significant ($r_{sp} = -0.58$, $p = 0.0001$; $T_{2m}(\text{ms}) = -(16.8 \pm 5.2) \times G(\text{Pa}) + (928 \pm 97)$)

for all the analysed samples. Even though considering separately the samples before and after chest physiotherapy, the same strong correlation is demonstrated too.

Thus, for what concerns the evaluation of lung functionality in relation to FEV_1 , both T_{2m} and T_{2mb} can be chosen as indicators of patient clinical conditions. Figure 5 shows the significant inverse correlation between T_{2m} and the shear modulus G on the samples both before and after chest

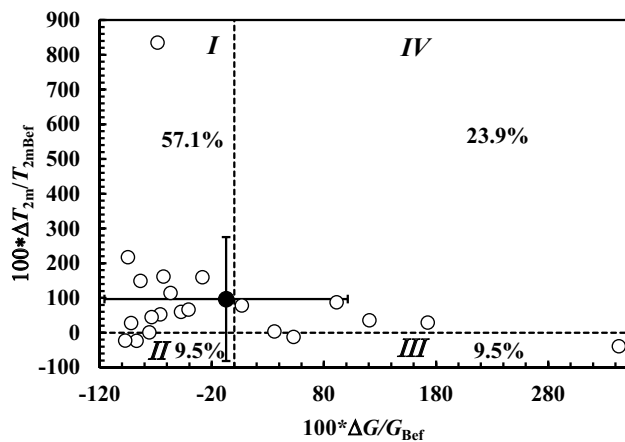


Fig. 6 Relative percentage variation of the relaxation time ($100 \times \Delta T_{2m} / T_{2mBef}$) versus the relative percentage variation of the shear modulus ($100 \times \Delta G / G_{Bef}$) considering samples after and before chest physiotherapy (open circles). Black circle indicates the average value of $100 \times \Delta T_{2m} / T_{2mBef}$ and $100 \times \Delta G / G_{Bef}$, while vertical and horizontal solid lines indicate the associated standard deviation in the vertical and horizontal direction

physiotherapy ($r_{sp} = -0.58$, $p = 0.0001$). These evidences support the beneficial effects of chest physiotherapy. Indeed, at fixed G , Fig. 5 shows that chest physiotherapy leads to a higher T_{2m} (see the solid and dashed lines in Fig. 5). An additional and conclusive proof of chest physiotherapy benefit is displayed in Fig. 6. This picture reports the %, relative (compared to the value before chest physiotherapy, T_{2mBef}) variation (ΔT_{2m}) of T_{2m} versus the %, relative (with respect to the value before chest physiotherapy, G_{Bef}) variation (ΔG) of G . It is possible to detect that in the 57.1% of the cases (section I in Fig. 6), chest physiotherapy leads to both an increase of T_{2m} and a decrease of G , which indicates the partial breakage of the original mucus polymeric network that yields to a weaker nanostructure. Indeed, the combination of Eqs. (3), (4) and (12) evidences that T_{2m} (or T_{2mb}) is inversely proportional to $G^{1/3}$. Therefore, network damaging is due to a T_{2m} increase, as per G decrease due to a reduction of crosslink density (see Eq. (3)). The direct correlation between T_{2m} and FEV_1 evidences that nanostructure variation indicates a better lung functionality. Figure 6, section IV shows that in the 23.9% of the cases, chest physiotherapy determines an increase both in T_{2m} and G . This behaviour could be explained assuming that the increase of sputum stiffness is not due to the increase of the crosslink density, but to the increase of polymeric fibres strength as the polymeric chains group into thicker fibres (see Fig. 6). This perfectly matches with G and T_{2m} increase, as T_{2m} rises with the decrease of the ratio between the solid (fibres) surface (S) in contact with water molecules and the hydrogel water molecule volume (V) as per Eq. (10) [22, 54].

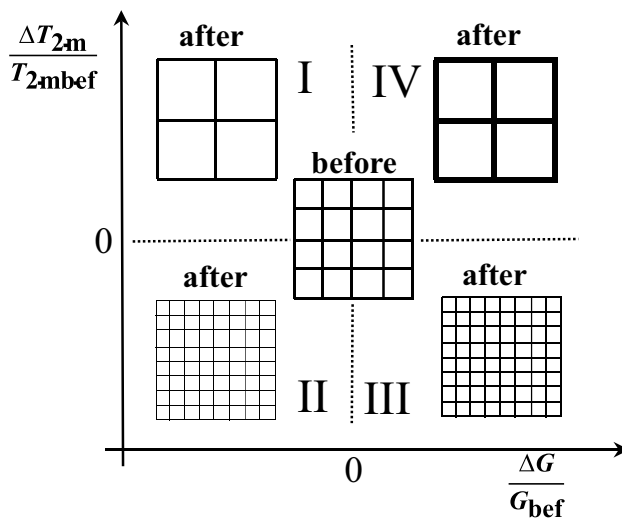


Fig. 7 Qualitative effect of chest physiotherapy on sputum nanostructure deduced by the percentage variation of the relaxation time ($100 \times \Delta T_{2m} / T_{2mbef}$) and the relative percentage variation of the shear modulus ($100 \times \Delta G / G_{bef}$) (sections I–IV are those of Fig. 6). Depending on the relative variation of T_{2m} and G , different mucus nanostructures can be supposed

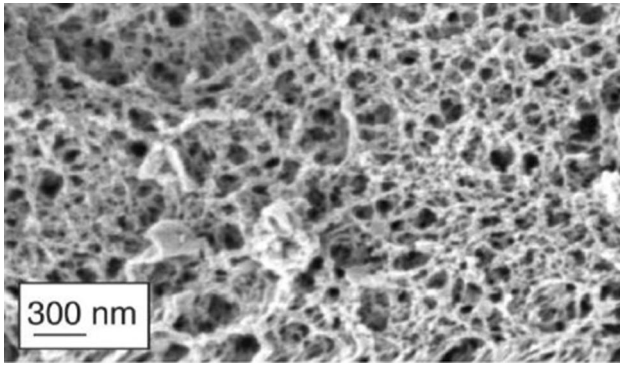


Fig. 8 Nanostructure of CF sputum. The complexity of CF nanostructure is increased by the presence of DNA, cell debris and bacteria (not visible in this figure). (Adapted from Ref [58] with permission from FutureScience)

Figure 6 section II reveals that in 9.5% of the cases, chest physiotherapy determines both G and T_{2m} reduction. This proves the increase of the crosslink density, which takes place among thinner and weaker fibres. In the 9.5% of the cases, chest physiotherapy determines a G increase and T_{2m} decrease (Fig. 6 section III). In this case, T_{2m} decrease and G increase could be related to mesh size reduction. Overall, the effect of chest physiotherapy on sputum nanostructure is positive, as it determines the average T_{2m} increase and the average G decrease (see the black dot in section I of Fig. 6). Figure 7 qualitatively sums up the effect of chest physiotherapy on the sputum nanostructure, based on the relative variations of T_{2m} and G shown in Fig. 6.

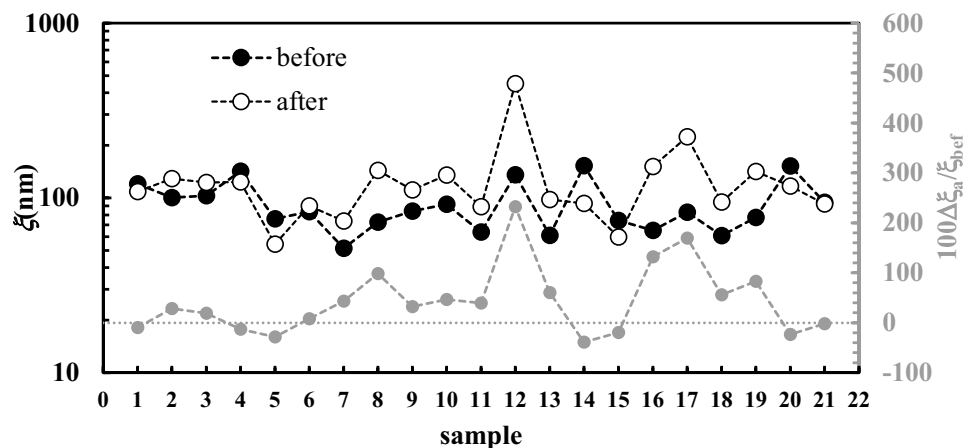
It is of utmost importance to remind that all the above considerations relay on the interpretation of experimental results in the light of Eqs. (3), (4) and (12). Thus, other experimental techniques (such as TEM/SEM or other image techniques) will be considered. However, the complex nature of CF sputum nanostructure, reported in Fig. 8, and the issues connected to the reliable acquisition and interpretation of images [55–57] make this task absolutely challenging.

Moreover, for what concerns the image analysis, the presence of DNA, cell debris and bacteria can create an extremely complex scenario. On the other hand, this is not a problem for the proposed combined approach (rheology and LF-NMR) as the presence of additional components just alters the S/V ratio (see Eq. (10)) that reflects in a variation of T_{2m} . Similarly, the presence of additional components affects the sputum rheological behaviour reflecting in alterations of G' (shall they represent physical or chemical bonds among different polymeric chains) or G'' (shall they stay in the sputum sol fraction). Thus, the presence of DNA, cell debris and bacteria is accounted for by our approach, and it is interpreted as a sort of network architecture modifications.

The general soundness of the presented approach is proved by Figs. 9 and 10 showing, respectively, the average mesh size (ξ_a) of all samples and the continuous mesh size distribution referring to sample 11 before and after chest physiotherapy (see Table 1 in Appendix 2). Indeed, according to Hanes and co-workers [58, 59], who applied a sophisticated particles tracking methods, the mesh size distribution of the CF sputum network ranges between 60 and 300 nm, with a mean value of (145 ± 50) nm. Figure 9 shows that, except for one case, ξ_a refers to the range of 50–250 nm, i.e. within the range indicated by Hanes and co-workers. Moreover, Fig. 10 shows that before chest physiotherapy (unperturbed sputum), the continuous mesh size distribution spans between 20 and 300 nm, perfectly matching Hanes and co-workers findings. Thus, the two different strategies (our bulk rheology-LF-NMR and Hanes' particle tracking) provide similar results.

Figure 9 also allows to sum up the effect of chest physiotherapy on sputum nanostructure. Indeed, Fig. 9 suggests that, on average, chest physiotherapy leads to an increase of ξ_a , as its relative variation ($100\Delta\xi_a/\xi_{bef}$) is mainly positive. Conversely, negative variations are limited in their amplitude (grey circles), with reference to positive ones (see dotted grey line). As per Eqs. (8) and (15), it is possible to determine the variation of the continuous mesh size distribution,

Fig. 9 Variation of the average mesh size (ξ_a) for the 21 samples considered (black circles, before chest physiotherapy; white circles after chest physiotherapy). Grey circles indicate the relative percentage variation of the average mesh size ξ_a (secondary vertical axis)



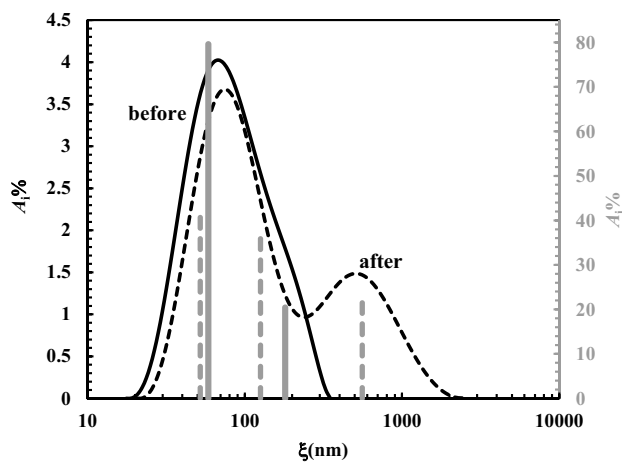


Fig. 10 Comparison between the continuous mesh size distribution before (solid black curve) and after (dashed black line) chest physiotherapy referring to samples 11 (see Table 1). Solid grey vertical lines (secondary vertical axis on the right) indicate the discrete mesh size distribution referring the solid black curve. Dashed grey vertical lines (secondary vertical axis on the right) indicate the discrete mesh size distribution referring the dashed black curve

based on chest physiotherapy treatment. Figure 10 shows, e.g. this comparison in the case of samples 11 (see Table 1 in Appendix 2).

It is possible to notice that chest physiotherapy pushes towards higher mesh size values (ξ) the entire mesh size distribution (compare the black solid line and dashed black line). It also provides for changes in the shape of the distribution, making more evident the second peak, which is just slightly visible before the treatment. This is a pivotal hallmark: the second peak, moving from, about, 200 nm to 500 nm, refers to mesh size range which is typical of healthy sputum.

Moreover, Fig. 10 clearly proves that about 20% of the mesh size distribution is on the normal range size (dashed black line), while, before chest physiotherapy (continuous solid line), 100% of the mesh size refers to the pathological range. Therefore, both before and after chest physiotherapy, the discrete mesh size distribution (grey vertical lines) results in a trend of the continuous one.

Drug delivery through mucus is a complex phenomenon which is on stage for researchers, with a main focus of the current COVID period the world is facing [16–18, 60]. For what concerns drug (e.g. antibiotics, anti-inflammatory and mucolytics) administration by inhalation and in order to achieve this task, detailed information about mesh size are of key importance. Indeed, the entire delivery process implies different steps such as drug deposition on ASL (airway surface liquid, sum of the periciliary liquid and mucus layers) and drug diffusion throughout it. Modern strategies ensure that within, about, 7 min, the administered aerosol can get the ASL [61, 62]. In the light of the simplifying hypotheses

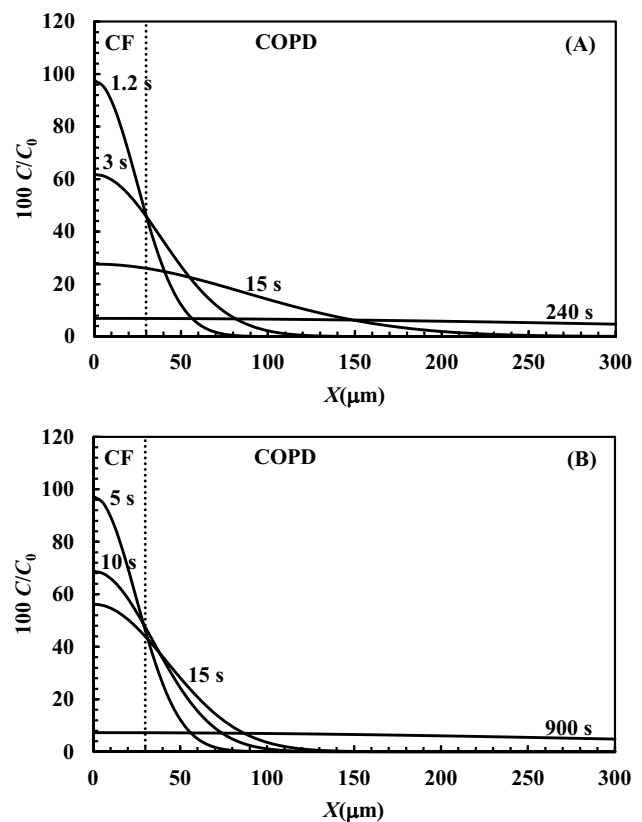


Fig. 11 Drug profile concentration (C/C_0 , solid line) inside ASL thickness at different times according to Eq. (16) assuming $\delta = 3 \mu\text{m}$. The drug diffusion coefficient has been evaluated according to Eq. (17) assuming $\varphi = 0.05$, $r_s = 1.1 \text{ nm}$, $D_0 = 3 \times 10^{-10} \text{ m}^2/\text{s}$ and **A** $Y = 3$ ($D = 2.5 \times 10^{-10} \text{ m}^2/\text{s}$) or **B** $Y = 30$ ($D = 0.6 \times 10^{-10} \text{ m}^2/\text{s}$)

on which Eq. (16) relies, we would like to simulate the kinetics of the drug diffusion process inside ASL. At this purpose, the drug diffusion coefficient D was evaluated according to Eq. (17) assuming the values of the model parameters ($\varphi = 0.05$, $r_s = 1.1 \text{ nm}$, $D_0 = 3 \times 10^{-10} \text{ m}^2/\text{s}$) presented in the “Diffusion” section. Moreover, the average mesh size was fixed equal to the average value (92 nm) reported in Table 1; Y was set equal to 3 or 30 to account for two limiting conditions and $\delta = 3 \mu\text{m}$. When $Y = 3$ (this corresponding to a higher drug diffusivity $D = 2.5 \times 10^{-10} \text{ m}^2/\text{s}$), Fig. 11A reveals that within few seconds, the drug can cross the ASL typical thickness of healthy subjects and CF patients ($\approx 30 \mu\text{m}$).

Indeed, the dimensionless concentration C/C_0 achieves about 50% of the initial solution concentration at the ASL bottom in a very short time (see the profile concentration curves labelled 1.2 and 3 s in Fig. 11A). For longer times, the C/C_0 profile assumes a flatter shape (see the 15 s labelled curve in Fig. 11A) and a uniform distribution is achieved after 240 s through the ASL thickness competing to COPD (chronic obstructive pulmonary diseases) patients (300 μm). COPD has been considered as it is due to an acquired

CFTR impairment, resulting in increased lung mucus viscosity similarly to CF. Considering $Y=30$, this value represents a lower value of the diffusion coefficient ($D=0.6 \times 10^{-10} \text{ m}^2/\text{s}$). Figure 11B reveals that the diffusion process is slowed down, but C/C_0 is about 50% at a penetration depth of $30 \mu\text{m}$ after 5 s. Moreover, 900 s are required to get a flat concentration profile up to $300 \mu\text{m}$, i.e. the ASL thickness which can be detected in COPD patients. Thus, in the case of CF patients, these simulations indicate that the drug can diffuse on the ASL thickness in a few seconds. On the other hand, in the case of COPD patients, 6–15 min are required to get the same effect if ASL thickness is about $300 \mu\text{m}$. It is worth to mention that the values of the diffusion coefficients therein reported, assuming $Y=3$ or 30 ($2.5 \times 10^{-10} \text{ m}^2/\text{s}$ and $0.6 \times 10^{-10} \text{ m}^2/\text{s}$, respectively), approximately represent the maximum and minimum D range which can be determined by the experimental permeability data through mucus performed by Bhat and co-workers [17, 18] that span from $2.4 \times 10^{-10} \text{ m}^2/\text{s}$ down to $0.7 \times 10^{-10} \text{ m}^2/\text{s}$.

In the case of CF patients, drug diffusion through mucus is not the rate determining step of the whole delivery process. In the worst conditions for COPD patients, drug diffusion can be compared to the inhalation time. However, in both cases, the time required for drug diffusion is short, this witnessing the promising role of inhalation to match pulmonary diseases.

Conclusions

The characterization of the sputum of CF by the combined use of rheology and *LF-NMR* allowed getting information about the nanostructure of sputum derived from the mucus lining the bronchial tree. In particular, this analysis was aimed to determine sputum nanostructure variations, as a result of chest physiotherapy, a routine procedure adopted in CF patients. We could verify that significant nanostructure variations occurred upon chest physiotherapy, leading to beneficial clinical effects for the patients. Interestingly, the combined use of rheology and *LF-NMR* allowed to define the nanostructure characteristics that each technique (if used singularly) would have never been able to provide.

Moreover, assuming that drugs diffuse inside mucus according to Fick's law, as well as in the sputum nanostructure, we could determine that in the case of healthy subjects and CF patients, about 7 min from inhalation are needed to get the drug active inside the mucus, i.e. a very short time. In case of COPD patients, this time has been estimated to about 15 min in the worst situation ($300 \mu\text{m}$ ASL thickness). Anyway, in both cases, the time required to get drug action since inhalation resulted to be short. Therefore, the inhalation delivery demonstrated a key role to provide for effective info about pulmonary diseases, such as those afflicting CF and COPD patients.

Author contribution M. Abrami, M. Maschio, M. Conese, M. Confalonieri, M. Grassi and G. Grassi conceived the paper. M. Grassi, G. Grassi and G. Milcovich wrote the paper with the support of M. Maschio, M. Grassi and G. Grassi. G. Milcovich and A. Biasin took care of text critical revision, re-editing and re-writing. M. Conese, M. Confalonieri, M. Abrami and C. Fornasier executed the experimental tests. A. Adrover took care of all the statistical aspects. F. Gerin took care of sample collection, storing and transfer to the LF-NMR laboratory. F. Salton, B. Dapas and R. Farra ensured the connection between the different laboratories involved and critically reviewed paper draft. All authors equally contributed to the definition of the experimental plan.

Funding Open access funding provided by Università degli Studi di Trieste within the CRUI-CARE Agreement. This paper has been financed by *Fondazione CRT Trieste* project n°103069 and by the so-called Programma di valorizzazione dei brevetti del sistema universitario del Friuli Venezia Giulia, Unity FVG PoC, 2020, Italy.

Availability of data and materials Where not directly provided in the paper, all the data referring to this paper are available upon request to the corresponding author.

Declarations

Ethics approval and consent to participate Sputum samples were provided by the Burlo Garofolo Hospital, following a procedure approved by the Ethics Committee (prot n. 496/2916, CI M-11, 22–3-2016). Written informed consent was obtained from each patient.

Consent for publication Not applicable.

Competing interests The authors declare no competing interests.

Appendix 1

The approximation of the Scherer theory [33] by Abrami and co-workers [34] allows to provide a simple relation between the average mesh size ξ_a , the polymer volume fraction ϕ and the polymeric chains radius r_f :

$$\xi_a = r_f \sqrt{\frac{C_1}{C_0} \frac{1-0.58\phi}{\phi}} \tag{18}$$

where C_1 and C_0 are two constants depending on the network architecture (cubical, tetrahedral or octahedral) whose values are defined by the Scherer theory ([33]; for a cubical network, $C_0=1$ and $C_1=3\pi$). The combination of Eq. (18) and Eq. (17) allows expressing the ratio D/D_0 as function of the polymer volume fraction (ϕ) or the average mesh size (ξ_a):

$$\frac{D}{D_0} = \left(1 - \frac{2r_s/r_f}{\sqrt{\frac{C_1}{C_0} \frac{1-0.58\phi}{\phi}}}\right) e^{-Y(\frac{\phi}{1-\phi})} \tag{19}$$

$$\frac{D}{D_0} = \left(1 - \frac{2}{\xi_a^+}\right) e^{-\left(\frac{Y}{(\xi_a^+ \frac{r_s}{r_f})^2 \frac{C_0}{C_1} - 0.42}\right)} \quad \xi_a^+ = \frac{\xi_a}{r_s} \tag{20}$$

Figure 12, Eq. (18) shows Eqs. (19) and (20) trend assuming different values of the ratio r_s/r_f .

The advantage connected with the use of these equations consists in the possibility of simultaneously accounting for both the effect of volume fraction and average mesh size on drug diffusivity, an aspect, usually not explicitly dealt with in literature.

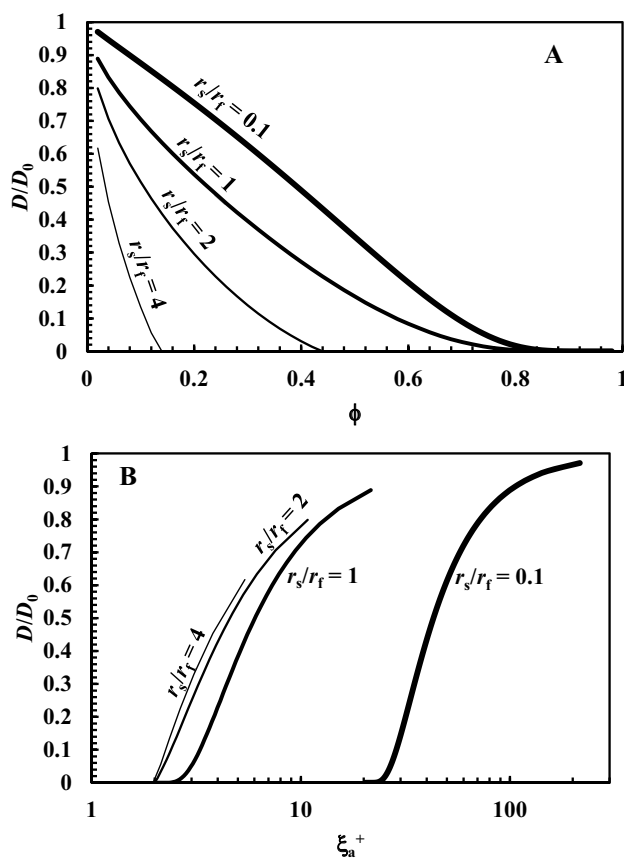


Fig. 12 A Variation of the ratio D/D_0 according to Eq. (18) and B Eq. (19) assuming different values of the ratio between the drug molecule radius (r_s) and the radius (r_f) of the fibres constituting the polymeric network pervading the hydrogel. These simulation refer to a cubical mesh organization ($C_0=1$; $C_1=3\pi$ [33])

Appendix 2

Table 1 Shear modulus (G), average mesh size (ξ_a), average value of the inverse relaxation time ($(1/T_2)_m$), and percentage ($A_{1\%}$) of the different relaxation times T_{2i} and mesh size ξ_i

Sample	$G(\text{Pa})$	ξ_a (nm)	$(1/T_2)_m \text{ ms}^{-1}$	$A_{1\%}$	$T_{2i}(\text{ms})$	$\xi_i(\text{nm})$
<i>Before chest physiotherapy</i>						
1	4.5	120	1.767×10^{-3}	17.5	2182	961
				42.8	798	183
				39.7	344	68
2	7	100	4.079×10^{-3}	19.4	612	280
				65.8	261	107
				14.8	119	47
3	7.2	103	1.278×10^{-3}	43.6	2095	501
				41.3	775	102
				15.1	281	31
4	2.7	142	1.379×10^{-3}	34.5	1463	429
				43.9	730	161
				21.6	292	56
5	18	76	4.360×10^{-3}	6.9	955	400
				42.6	365	125
				50.5	162	52
6	15	83	2.910×10^{-3}	31.5	511	130
				68.5	299	71
				56.9	261	71
7	58	51	5.200×10^{-3}	43.1	143	38
				32.9	1218	222
				51.6	575	83
8	21	72	1.952×10^{-3}	15.5	197	25
				24.2	1047	362
				42.6	435	122
9	13	84	3.219×10^{-3}	33.2	165	43
				21.5	330	212
				78.5	131	79
10	10	92	6.645×10^{-3}	20.4	355	169
				79.6	124	55
				53.7	2780	1089
11	30	64	7.014×10^{-3}	29.4	989	131
				16.9	341	36
				22.7	866	155
12	3	135	0.985×10^{-3}	71.0	389	60
				6.3	145	21
				16.7	1831	956
13	34	61	2.523×10^{-3}	45.3	861	296
				32.3	364	106
				5.7	117	32
14	2	153	1.994×10^{-3}	40.7	502	136
				50.9	270	68
				8.4	115	28
15	19	74	3.434×10^{-3}	39.4	935	116
				60.6	476	51
				10.5	2033	830
16	28	65	1.692×10^{-3}	62.0	571	124
				27.5	204	40
17	14	83	2.486×10^{-3}			

Table 1 (continued)

Sample	$G(\text{Pa})$	ξ_a (nm)	$(1/T_2)_m \text{ms}^{-1}$	$A_{1\%}$	$T_{2i}(\text{ms})$	$\xi_i(\text{nm})$
18	35	61	4.729×10^{-3}	8.4	632	206
				70.2	248	72
				21.4	121	34
19	17	77	6.794×10^{-3}	13.1	353	197
				52.7	133	70
				34.2	139	73
20	2	152	2.936×10^{-3}	18.4	680	338
				62.6	384	174
				19.0	183	78
21	10	94	3.462×10^{-3}	21.1	875	345
				55.3	343	114
				23.6	147	46
<i>After chest physiotherapy</i>						
1	6	108	1.494×10^{-3}	15.0	2191	716
				52.8	828	142
				32.2	408	61
2	3.7	100	2.926×10^{-3}	20.5	1108	541
				44.6	441	171
				34.9	202	73
3	4.3	122	0.518×10^{-3}	86.0	2322	189
				14.0	946	38
				38.3	1463	429
4	4.2	142	1.708×10^{-3}	32.4	730	161
				29.3	292	56
				14.1	1224	428
5	49.5	54	4.576×10^{-3}	22.5	483	130
				45.4	205	51
				18.0	101	24
6	11	90	1.371×10^{-3}	30.5	1632	289
				60.2	699	85
				9.3	287	31
7	19.6	74	3.628×10^{-3}	23.5	500	143
				66.7	288	77
				9.8	116	30
8	2.6	144	2.435×10^{-3}	20.0	1117	498
				61.0	492	177
				19.0	187	61
9	5.7	84	1.657×10^{-3}	36.4	1924	618
				33.8	812	160
				29.8	283	47
10	3.2	135	0.763×10^{-3}	57.2	2067	312
				36.6	1152	111
				6.2	368	27
11	11	89	3.903×10^{-3}	21.5	1176	557
				37.6	352	126
				40.9	154	52
12	0.1	450	1.311×10^{-3}	36.1	2439	3364
				35.7	1194	827
				21.9	487	263
				6.3	152	74

Table 1 (continued)

Sample	G(Pa)	ξ_a (nm)	$(1/T_2)_m$ ms ⁻¹	A _{1%}	T _{2i} (ms)	ξ_i (nm)
13	8.4	98	2.210×10^{-3}	46.2	628	143
				53.8	365	77
14	9.7	93	2.425×10^{-3}	14.7	979	267
				67.5	477	110
				17.8	207	44
15	36.8	60	2.197×10^{-3}	18.0	1540	304
				47.8	609	84
				34.2	264	33
16	2.3	151	1.399×10^{-3}	9.5	1797	597
				45.4	968	224
				45.1	514	102
17	0.7	223	0.554×10^{-3}	72.6	2296	384
				27.4	1153	106
18	9.3	94	3.288×10^{-3}	66.0	342	107
				17.7	667	232
				16.3	149	44
19	2.7	142	2.818×10^{-3}	42.8	581	249
				57.2	275	107
20	4.9	117	2.027×10^{-3}	73.8	627	155
				26.2	308	69.0
21	10.4	92	2.155×10^{-3}	32.5	1386	386
				46.0	509	103
				21.5	211	39

Open Access This article is licensed under a Creative Commons Attribution 4.0 International License, which permits use, sharing, adaptation, distribution and reproduction in any medium or format, as long as you give appropriate credit to the original author(s) and the source, provide a link to the Creative Commons licence, and indicate if changes were made. The images or other third party material in this article are included in the article's Creative Commons licence, unless indicated otherwise in a credit line to the material. If material is not included in the article's Creative Commons licence and your intended use is not permitted by statutory regulation or exceeds the permitted use, you will need to obtain permission directly from the copyright holder. To view a copy of this licence, visit <http://creativecommons.org/licenses/by/4.0/>.

References

- Farrell PM. The prevalence of cystic fibrosis in the European Union. *J Cyst Fibros*. 2008;7:450–3. <https://doi.org/10.1016/j.jcf.2008.03.007>.
- Ciofu O, Tolker-Nielsen T, Jensen PO, Wang H, Hoiby N. Antimicrobial resistance, respiratory tract infections and role of biofilms in lung infections in cystic fibrosis patients. *Adv Drug Deliv Rev*. 2015;85:7–23. <https://doi.org/10.1016/j.addr.2014.11.017>.
- Cystic Fibrosis Foundation Patient Registry 2014 Annual Data Report, Bethesda, Maryland, 2015 Cystic Fibrosis Foundation; Cystic Fibrosis Foundation Patient Registry 2019 Annual Data Report, Bethesda, Maryland, 2020 Cystic Fibrosis Foundation.
- Emerson J, Rosenfeld M, McNamara S, Ramsey B, Gibson RL. *Pseudomonas aeruginosa* and other predictors of mortality and morbidity in young children with cystic fibrosis. *Pediatr Pulmonol*. 2002;34:91–100. <https://doi.org/10.1002/ppul.10127>.
- Fyfe JA, Govan JR. Alginate synthesis in mucoid *Pseudomonas aeruginosa*: a chromosomal locus involved in control. *J Gen Microbiol*. 1980;119:443–50. <https://doi.org/10.1099/00221287-119-2-443>.
- Govan JR, Deretic V. Microbial pathogenesis in cystic fibrosis: mucoid *Pseudomonas aeruginosa* and *Burkholderia cepacia*. *Microbiol Rev*. 1996;60:539–74. <https://doi.org/10.1128/mmb.60.3.539-574.1996>.
- Folkesson A, Jelsbak L, Yang L, Johansen HK, Ciofu O, Hoiby N, Molin S. Adaptation of *Pseudomonas aeruginosa* to the cystic fibrosis airway: an evolutionary perspective. *Nat Rev Microbiol*. 2012;10:841–51. <https://doi.org/10.1038/nrmicro2907>.
- Posocco B, Dreussi E, de Santa J, Toffoli G, Abrami M, Musiani F, Grassi M, Farra R, Tonon F, Grassi G, Daps B. Polysaccharides for the delivery of antitumor drugs. *Materials*. 2015;8:2569–651. <https://doi.org/10.3390/ma8052569>.
- Yang D, Jones KS. Effect of alginate on innate immune activation of macrophages. *J Biomed Mater Res A*. 2009;90:411–8. <https://doi.org/10.1002/jbm.a.32096>.
- Iwamoto M, Kurachi M, Nakashima T, Kim D, Yamaguchi K, Oda T, Iwamoto Y, Muramatsu T. Structure–activity relationship of alginate oligosaccharides in the induction of cytokine production from RAW264.7 cells. *FEBS Lett*. 2005;579:4423–29. <https://doi.org/10.1016/j.febslet.2005.07.007>.
- Cobb LM, Mychaleckyj JC, Wozniak DJ, Lopez-Boado YS. *Pseudomonas aeruginosa* flagellin and alginate elicit very distinct gene expression patterns in airway epithelial cells: implications for cystic fibrosis disease. *J Immunol*. 2004;173:5659–70. <https://doi.org/10.4049/jimmunol.173.9.5659>.
- Lai SK, Wang YY, Wirtz D, Hanes J. Micro- and macrorheology of mucus. *Adv Drug Deliv Rev*. 2009;61(2):86–100. <https://doi.org/10.1016/j.addr.2008.09.012>.

13. Dawson M, Wirtz D, Hanes J. Enhanced viscoelasticity of human cystic fibrotic sputum correlates with increasing microheterogeneity in particle transport. *J Biol Chem.* 2003;278(50):50393–401. <https://doi.org/10.1074/jbc.M309026200>.
14. Duncan GA, Jung J, Joseph A, Thaxton AL, West NE, Boyle MP, Hanes J, Suk JS. Microstructural alterations of sputum in cystic fibrosis lung disease. *JCI Insight.* 2016;1(18): e88198. <https://doi.org/10.1172/jci.insight.88198>.
15. Lai SK, Wang YY, Hida K, Cone R, Justin HJ. Nanoparticles reveal that human cervicovaginal mucus is riddled with pores larger than viruses. *PNAS.* 2010;107(2):598–603. <https://doi.org/10.1073/pnas.0911748107>.
16. Bhat PG, Flanagan DR, Donovan MD. The limiting role of mucus in drug absorption: drug permeation through mucus solution. *Int J Pharm.* 1995;126:179–87. [https://doi.org/10.1016/0378-5173\(95\)04120-6](https://doi.org/10.1016/0378-5173(95)04120-6).
17. Bhat PG, Flanagan DR, Donovan MD. Drug binding to gastric mucus glycoproteins. *Int J Pharm.* 1996;134:15–25. [https://doi.org/10.1016/0378-5173\(95\)04333-0](https://doi.org/10.1016/0378-5173(95)04333-0).
18. Bhat PG, Flanagan DR, Donovan MD. Drug diffusion through cystic fibrotic mucus: steady-state permeation, rheologic properties, and glycoprotein morphology. *J Pharm Sci.* 1996;85:624–30. <https://doi.org/10.1021/js950381s>.
19. McIlwaine M, Button B, Dawn K. Positive expiratory pressure physiotherapy for airway clearance in people with cystic fibrosis. *Cochrane Database Syst Rev.* 2015; 6: CD003147. <https://doi.org/10.1002/14651858.CD003147.pub4>.
20. Lapasin R, Priel S. Rheology of industrial polysaccharides: theory and applications. Springer Verlag, chapter. 1995;3:162–249. <https://doi.org/10.1007/978-1-4615-2185-3>.
21. Draper NR, Smith H. Applied regression analysis. New York: John Wiley & Sons Inc; 1966.
22. Abrami M, Marizza P, Zecchin F, Paolo Bertocin P, Marson D, Lapasin R, de Riso F, Posocco P, Grassi G, Grassi M. Theoretical importance of PVP-alginate hydrogels structure on drug release kinetics. *Gels.* 2019;5(2):22. <https://doi.org/10.3390/gels5020022>.
23. Flory PJ. The thermodynamics of polymer solutions. In: Principles of Polymer Chemistry. Cornell University Press, Ithaca, N.Y., 469–470. 1953.
24. Schurz J. Rheology of polymer solutions of the network type. *Prog Polym Sci.* 1991;16:1–53. [https://doi.org/10.1016/0079-6700\(91\)90006-7](https://doi.org/10.1016/0079-6700(91)90006-7).
25. Brownstein KR, Tarr CE. Importance of classical diffusion in NMR studies of water in biological cells. *Phys Rev A.* 1979; 19(6):2446–53.
26. Chui MM, Phillips RJ, McCarthy MJ. Measurement of the porous microstructure of hydrogels by nuclear magnetic resonance. *J Colloid Interface Sci.* 1995;174(2):336–44. <https://doi.org/10.1006/jcis.1995.1399>.
27. Whittall KP, MacKay AL. Quantitative interpretation of NMR relaxation data. *J Magn Reson.* 1989;84:134–52. [https://doi.org/10.1016/0022-2364\(89\)90011-5](https://doi.org/10.1016/0022-2364(89)90011-5).
28. Provencher SWA. A constrained regularization method for inverting data represented by linear algebraic or integral equations. *Comput Phys Comm.* 1982;27:213–27. [https://doi.org/10.1016/0010-4655\(82\)90173-4](https://doi.org/10.1016/0010-4655(82)90173-4).
29. Wang X, Ni Q. Determination of cortical bone porosity and pore size distribution using a low field pulsed NMR approach. *J Orthop Res.* 2003;21:312–9. [https://doi.org/10.1016/S0736-0266\(02\)00157-2](https://doi.org/10.1016/S0736-0266(02)00157-2).
30. Coviello T, Matricardi P, Alhaique F, Farra R, Tesi G, Fiorentino S, Asaro F, Milcovich G, Grassi M. Guar gum/borax hydrogel: rheological, low field NMR and release characterizations. *eXPRESS Polym Lett.* 2013;7, 733–46. <https://doi.org/10.3144/expresspolymlett.2013.71>.
31. Abrami M, Siviello C, Grassi G, Larobina D, Grassi M. Investigation on the thermal gelation of chitosan/ β -glycerophosphate solutions. *Carbohydr Polym.* 2019;214:110–6. <https://doi.org/10.1016/j.carbpol.2019.03.015>.
32. Kopac T, Abrami M, Grassi M, Rucigaj A, Krajnc M. Polysaccharide-based hydrogels crosslink density equation: a rheological and LF-NMR study of polymer-polymer interaction. *Carbohydr Polym.* 2022;277, 118895, 1–15. <https://doi.org/10.1016/j.carbpol.2021.118895>.
33. Scherer GW. Hydraulic radius and mesh size of gels. *J Sol-Gel Sci Techn.* 1994;1:285–91. <https://doi.org/10.1007/BF00486171>.
34. Abrami M, Chiarappa G, Farra R, Grassi G, Marizza P, Grassi M. Use of low field NMR for the characterization of gels and biological tissues. *ADMET & DMPK.* 2018;6:34–46. <https://doi.org/10.5599/admet.6.1.430>.
35. Holz M, Heil SR, Sacco A. Temperature-dependent self-diffusion coefficients of water and six selected molecular liquids for calibration in accurate ^1H NMR PFG measurements. *Phys Chem Chem Phys.* 2000;2:4740–2. <https://doi.org/10.1039/b005319h>.
36. Meiboom S, Gill D. Modified spin-echo method for measuring nuclear relaxation times. *Rev Sci Instrum.* 1958;29(8):688–91. <https://doi.org/10.1063/1.1716296>.
37. Manolidis M, Isabey D, Louis B, Grotberg JB, Filoche M. A Macroscopic Model for simulating the mucociliary clearance in a bronchial bifurcation: the role of surface tension. *J Biomed Eng.* 2016;138(121005):1–8. <https://doi.org/10.1115/1.4034507>.
38. Derichs N, Jin BJ, Song Y, Finkbeiner WE, Verkman AS. Hyper-viscous airway periciliary and mucous liquid layers in cystic fibrosis measured by confocal fluorescence photobleaching. *The FASEB J Res Commun.* 2011;(25), 2325–32. <https://doi.org/10.1096/fj.10-179549>.
39. Abrami M, Ascenzioni F, Di Domenico EG, Maschio M, Ventura A, Confalonieri M, Di Gioia S, Conese M, Dapas B, Grassi G, Grassi M. A Novel Approach based on low-field NMR for the detection of the pathological components of sputum in cystic fibrosis patients. *Magn Reson Med.* 2018;79:2323–31. <https://doi.org/10.1002/mrm.26876>.
40. King M. S. Physiology of mucus clearance. *Paediatr Respir Rev.* 2006;7S:S212–4. <https://doi.org/10.1016/j.prrv.2006.04.199>.
41. Ren S, Li W, Wang L, Shi Y, Cai M, Hao L, Luo Z, Niu J, Xu W, Luo Z. Numerical analysis of airway mucus clearance effectiveness using assisted coughing techniques. *Sci Rep.* 2020;(10), 2030, 1–10. <https://doi.org/10.1038/s41598-020-58922-7>.
42. Saxena A, Kumar V, Shukla JB. Four layer cylindrical model of mucus transport in the lung: effect of prolonged cough. *Bangladesh J Med Sci.* 2020;19:53–63. <https://doi.org/10.3329/bjms.v19i1.43873>.
43. Grassi M, Grassi G. Application of mathematical modeling in sustained release delivery systems. *Expert Opin Drug Deliv.* 2014;11:1299–321. <https://doi.org/10.1517/17425247.2014.924497>.
44. Lustig SR, Peppas NA. Solute diffusion in swollen membranes. IX. Scaling laws for solute diffusion in gels. *J Appl Polym Sci.* 1988;36, 735–47. <http://dx.doi.org/10.1002/app.1988.070360401>.
45. Amsden B. Solute diffusion within hydrogels. Mechanisms and models *Macromolecules.* 1998;31:8382–95. <https://doi.org/10.1021/ma980765f>.
46. Dalmoro A, Barba AA, Lamberti G, Grassi M, d'Amore M. Pharmaceutical applications of biocompatible polymer blends containing sodium alginate. *Adv Polym Technol.* 2012;31:219–30. <https://doi.org/10.1002/adv.21276>.
47. Samet JM, Cheng WP. The role of airway mucus in pulmonary toxicology. *Environ Health Perspect.* 1994;102 (Suppl 2), 89–103. <http://dx.doi.org/10.1289/ehp.9410289>.
48. Benke E, Farkas A, Imre BI, Szabo-Revesz P, Ambrus R. Stability test of novel combined formulated dry powder inhalation system

- containing antibiotic: physical characterization and in vitro–in silico lung deposition results. *Drug Develop Ind Pharm.* 2019;45:1369–78. <https://doi.org/10.1080/03639045.2019.1620268>.
49. Meulemans A, Paycha F, Hannoun P, Vulpillat M. Measurements and clinical pharmacokinetic implications of diffusion coefficient of antibiotics in tissues. *Antimicrob Agents Chemother.* 1989;(33), 1286–90. <https://doi.org/10.1128/AAC.33.8.1286>.
50. Soriano AN, Bonifacio PB, Adamos KG, Adornado AP. Prediction of self-diffusion coefficients of ions from various livestock antibiotics in water at infinite dilution. *Earth Environ Sci.* 2018;(191) 012092IOP, 1 – 10. <https://doi.org/10.1088/1755-1315/191/1/012092>.
51. Rajendran RR, Banerjee A. Mucus transport and distribution by steady expiration in an idealized airway geometry. *Med Eng Phys.* 2019;66:26–39. <https://doi.org/10.1016/j.medengphy.2019.02.006>.
52. Olivença DV, Fonseca LL, Voit EO, Pinto FR. Thickness of the airway surface liquid layer in the lung is affected in cystic fibrosis by compromised synergistic regulation of the ENaC ion channel. *J R Soc Interface.* 2019;16:20190187. <https://doi.org/10.1098/rsif.2019.0187>.
53. Abrami M, Maschio M, Conese M, Confalonieri M, Di Gioia S, Gerin F, Dapas B, Tonon F, Farra R, Murano R, Zanella G, Salton F, Grassi G, Grassi M. Use of low field nuclear magnetic resonance to monitor lung inflammation and the amount of pathological components in the sputum of cystic fibrosis patients. *Magn Reson Med.* 2020;(84): 427 – 36. <https://doi.org/10.1002/mrm.28115>.
54. Maestri CA, Abrami M, Hazan S, Chisté E, Golan Y, Rohrer J, Bernkop-Schnürch A, Grassi M, Scarpa M, Bettotti P. Role of sonication pre-treatment and cation valence in the sol-gel transition of nano-cellulose suspensions. *Sci Rep.* 2017;7:11129. <https://doi.org/10.1038/s41598-017-11649-4>.
55. Wei Z, Gourevich I, Lora FL, Coombs N, Eugenia KE. TEM imaging of polymer multilayer particles: advantages, limitations, and artifacts. *Macromolecules.* 2006;39:2441–4. <https://doi.org/10.1021/ma052029z>.
56. Monsegue N, Reynolds WT, Jr., Hawk J. A., Murayama M. How TEM projection artifacts distort microstructure measurements: a case study in a 9 pct Cr-Mo-V steel. *Metall and Mater Trans A.* 2014;45A:3708–13. <https://doi.org/10.1007/s11661-014-2331-0>.
57. Gregersen SB, Glover ZJ, Wiking L, Cohen SA, C., Bertelsen K., Pedersen B., Poulsen K. R., Andersen U., Hammershøj M. Microstructure and rheology of acid milk gels and stirred yoghurts – quantification of process-induced changes by auto- and cross correlation image analysis. *Food Hydrocolloids.* 2021;111(106269):1–7. <https://doi.org/10.1016/j.foodhyd.2020.106269>.
58. Suk JS, Lai SK, Boylan NJ, Dawson MR, Boyle MP, Hanes J. Rapid transport of muco-inert nanoparticles in cystic fibrosis sputum treated with N-acetyl cysteine. *Nanomedicine.* 2011;6:365–75. <https://doi.org/10.2217/nmm.10.123>.
59. Suk JS, Lai SK, Wang YY, Ensign LM, Zeitlin PL, Boyle MP, Hanes J. The penetration of fresh undiluted sputum expectorated by cystic fibrosis patients by non-adhesive polymer nanoparticles. *Biomaterials.* 2009;30:2591–7. <https://doi.org/10.1016/j.biomaterials.2008.12.076>.
60. Khanvilkar K, Donovan MD, Flanagan DR. Drug transfer through mucus. *Adv Drug Deliv Rev.* 2001;48:173–93. [https://doi.org/10.1016/s0169-409x\(01\)00115-6](https://doi.org/10.1016/s0169-409x(01)00115-6).
61. Maselli DJ, Keyt H, Restrepo MI. Inhaled antibiotic therapy in chronic respiratory diseases. *Int J Mol Sci.* 2017;(18), 1062, 1–23. <http://dx.doi.org/10.3390/ijms18051062>.
62. Sorino C, Negri S, Spanevello A, Visca D, Scichilone N. Inhalation therapy devices for the treatment of obstructive lung diseases: the history of inhalers towards the ideal inhaler. *Eur J Intern Med.* 2020;75:15–8. <https://doi.org/10.1016/j.ejim.2020.02.023>.

Publisher's Note Springer Nature remains neutral with regard to jurisdictional claims in published maps and institutional affiliations.